Proceedings of the 21st ICSMGE, Vienna, Austria, 14 – 19 June 2026. Pistrol, Adam & Schweiger (eds.)
Published by: ÖGG, Austrian Society for Geomechanics, Salzburg, Austria, ISBN 978-3-9503898-4-5
https://doi.org/10.53243/ICSMGE2026-589

Effect of principal stress rotation on the thermal conductivity of granular materials

Wenbin Fei, Fei Wang
College of Civil Engineering, Hunan University, Changsha, Hunan, 410082, China, wenbinfei@hnu.edu.cn

ABSTRACT: Transportation loading on frozen soil foundations and compressed air energy storage systems both encounter challenges involving principal stress rotation (PSR) coupled with thermal transfer phenomena. While existing research has well documented the significant volumetric strains caused by PSR and their potential impact on soil thermal properties, investigations into particulate materials' thermal conductivity under PSR conditions remain scarce. This research employs discrete element method simulations incorporating a thermal conductance network model to analyze silica glass beads, specifically examining how stress parameters (intermediate principal stress coefficient b, mean principal stress p) and microstructural characteristics (porosity n, particle size ratio $d_{\max}/d_{\min}$) govern thermal conduction during PSR. Key findings demonstrate consistent shear-induced contraction regardless of stress parameters and microstructural characteristics, with cyclic PSR enhancing effective thermal conductivity (k_{eff}). Directional analysis shows k_{eff} in Z/Y directions decreases with higher b values while X-direction values increase, whereas elevated p and $d_{\max}/d_{\min}$ or reduced n universally boost k_{eff} across all axes. At the microstructural level, PSR drives the conversion of solid-fluid-solid thermal conduction paths to solid-solid paths, improving overall thermal performance without altering the total conduction path count. These insights provide valuable design considerations for granular material thermal management in geotechnical applications.

KEYWORDS: Principal stress rotation, Non-coaxia, Thermal conductance network model, Effective thermal conductivity.

1 INTRODUCTION

Principal stress rotation (PSR) describes the continuous angular deviation of principal stress directions from their initial state under dynamic loading. This phenomenon can influence soil and rock thermal conductivity by modifying particle contacts and bulk density—key factors governing heat transfer (Fei and Narsilio, 2022). Consequently, understanding PSR's thermal impact is vital in scenarios sensitive to temperature changes. Notable examples include:

(i) Performance of hybrid thermosyphons stabilizing frozen soil subgrades in cold regions (Zueter et al., 2021), where seasonal permafrost necessitates their installation (Figure 1a). The cyclic traffic loading inducing PSR might compromise hybrid thermosyphon efficiency.

(ii) Energy storage-release cycles in compressed air energy storage (CAES) systems (Liu et al., 2021). During CAES operations (Figure 1b), air charging/discharging induces PSR in cavern linings and surrounding rock, while associated temperature swings from air compression/expansion alter the rock's thermal regime (Zhou et al., 2025).

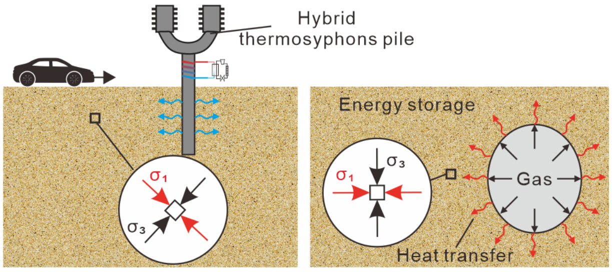

(a) (b)

Figure 1. Two scenarios involving principal stress rotation and thermal conductivity: (a) traffic load, and (b) energy storage and release.

These two cases collectively underscore PSR's potential effect on geomaterial heat conduction, highlighting the need for further research into its thermal performance implications across geotechnical applications.

This research utilizes the Discrete Element Method (DEM) and the Thermal Conductance Network Model (TCNM) to examine how PSR affects the thermal conductivity and anisotropy of granular assemblies. Initially, DEM simulations capture the mechanical response (including three-dimensional volumetric strain evolution) of spherical samples undergoing PSR. Subsequently, cubic sub-samples are extracted from these for thermal conductivity assessment. The study systematically explores the combined influence of PSR, stress conditions (e.g., intermediate principal stress ratio, mean principal stress), and microstructural characteristics (e.g., porosity, particle size distribution) on effective thermal conductivity.

2 THEORY AND METHODS

2.1 *Principal stress rotation*

A pure PSR test necessitates rotating the principal stress axes while maintaining constant principal stress magnitudes.

Figure 2(a~d) details the workflow for sample preparation and PSR simulation: (i) Initial deposition of a hexahedral sample under gravity. (ii) Extraction of a spherical specimen (radius is 2 cm) from the hexahedral assembly; surface particles are designated as the loading boundary, followed by isotropic consolidation under uniform stresses in all directions. (iii) Achievement of anisotropic consolidation by adjusting the magnitudes of the principal stresses. (iv) Synchronous rotation of the σ_1 and σ_3 directions around the Y-axis, keeping the magnitudes of all three principal stresses and the orientation of σ_2 constant.

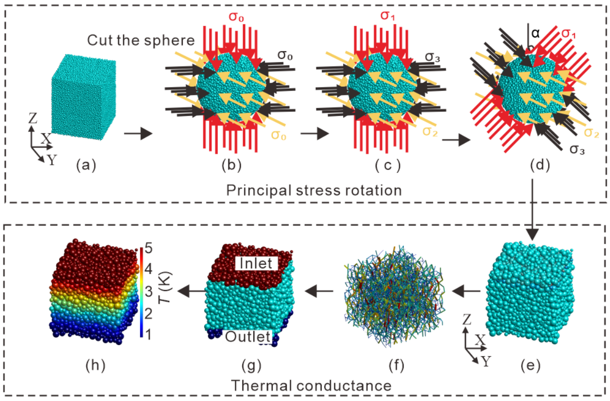

Figure 2. Simulation process (a) Gravity accumulation, (b) Isotropic consolidation, (c) Partial consolidation, (d) Principal stress rotation, (e) Cropped cube, (f) Thermal conductance network, (g) Set heat inlet and outlet, and (h) Heat transfer.

A complete rotation cycle corresponds to a 180° deflection angle α. The magnitude of α is defined as:

$$\alpha = \frac{1}{2}\arctan\left(\frac{2\tau_{\mathrm{ZX}}}{\sigma_{\mathrm{Z}} - \sigma_{\mathrm{X}}}\right) \tag{1}$$

Throughout the simulation, α is adjusted in 1° increments. The rotational velocity is regulated to guarantee quasi-static conditions, quantitatively verified using the inertial number:

$$I = \frac{\Delta\gamma}{\Delta t}\sqrt{\frac{\rho}{P_0}}d_{50} \tag{2}$$

where γ is the shear strain, Δt is the time step, ρ is the particle density, and P_0 is the mean principal stress, d_{50} is the mean particle diameter. It can be considered as quasi-static loading if $I < 10^{-3}$ (Cerfontaine et al., 2021).

2.2 *Thermal conductance network model*

Figure 2(e~h) illustrates the thermal conduction simulation workflow: (i) Following PSR completion, a cubic subsample is extracted from the spherical specimen. (ii) Particle coordinates and radii are utilized to construct a thermal network (detailed methodology follows). (iii) Temperature gradients are applied via defined heat inlets/outlets, (iv) Thermal conduction process is solved.

In the proposed methodology, the thermal conduction paths in fully saturated or dry specimens are simplified into two distinct mechanisms (Figure 3): solid-solid conduction (S-S) and solid-fluid-solid conduction (S-F-S). For particles in direct contact, the inter-center connection represents an S-S conduction path. When particles are non-contacting but separated by a gap distance smaller than half the equivalent radius ($0.5\mathrm{R}_{ij}$), the thermal transfer occurs through an S-F-S path. The equivalent radius R_{ij} can be calculated as:

$$R_{ij} = \frac{2R_iR_j}{R_i + R_j} \tag{3}$$

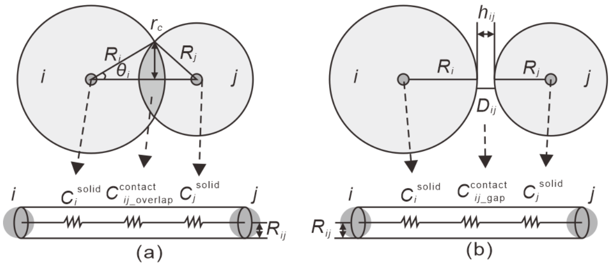

Figure 3. Schematic view of the two thermal conductance paths: (a) S-S conductance, and (b) S-F-S conductance.

The thermal conductivities of these two distinct paths are respectively denoted as $C_{ij\_\mathrm{overlap}}^{\mathrm{contact}}$ and $C_{ij\_\mathrm{gap}}^{\mathrm{contact}}$:

$$\begin{cases} C_{ij\_\mathrm{overlap}}^{\mathrm{contact}} = \pi k_{\mathrm{f}} R_{ij}\left[K_c + \Delta K_{\mathrm{g}} + \ln\left({k_{\mathrm{g}}}^2 / {k_{\mathrm{f}}}^2\right)\right] \\ K_{\mathrm{c}} = 2\beta_{ij} / \pi \text{ and } \Delta K_{\mathrm{g}} = -2\ln\left(\beta_{ij}\right),\ \text{if } \beta_{ij} \to \infty \\ K_{\mathrm{c}} = 0.22{\beta_{ij}}^2 \text{ and } \Delta K_{\mathrm{g}} = -0.05{\beta_{ij}}^2,\ \text{if } \beta_{ij} < 1 \\ \beta_{ij} = \dfrac{r_{\mathrm{c}} k_{\mathrm{g}}}{R_{ij} k_{\mathrm{f}}} \end{cases} \tag{4}$$

$$C_{ij\_\mathrm{gap}}^{\mathrm{contact}} = \begin{cases} \pi k_{\mathrm{f}} R_{ij} \ln\left({k_{\mathrm{g}}}^2 / {k_{\mathrm{f}}}^2\right),\ \text{if } \dfrac{h_{ij}{k_{\mathrm{g}}}^2}{R_{ij}{k_{\mathrm{f}}}^2} = 1 \\ \pi k_{\mathrm{f}} R_{ij} \ln\left(1 + \chi^2 R_{ij} / h_{ij}\right),\quad \text{otherwise} \end{cases} \tag{5}$$

where k_{f} and k_{g} are the thermal conductivities of the fluid and solid, r_{c} is the radius of the contact area (Figure 3a), and h_{ij} is the gap distance between the two contacting particles (Figure 3b).

The thermal conductance on each path encompasses three components: the solid conductance for particle i (C_i^{solid}), the solid conductance for particle j (C_j^{solid}), and the conductance for the heat transfer capacity between particle i and j ($C_{ij}^{\mathrm{contact}}$). The effective thermal conductance C_{ij}^{eff} on each path is:

$$C_{ij}^{\mathrm{eff}} = \left[\frac{1}{C_i^{\mathrm{solid}}} + \frac{1}{C_{ij}^{\mathrm{contact}}} + \frac{1}{C_j^{\mathrm{solid}}}\right]^{-1} \tag{6}$$

$$C_n^{\mathrm{solid}} = \pi k_{\mathrm{g}}(\chi R_{ij})^2 / R_n,\ n = i \text{ or } j \tag{7}$$

where R_n is the radius of particle i or j, and χ is the fraction of the mean curvature radius, generally taken as 0.5 (Yun and Evans, 2010).

The effective thermal conductivity (k_{eff}) on the cubic sample is:

$$k_{\mathrm{eff}} = \frac{L\sum q_{ij}}{A\left(T_{\mathrm{inlet}} - T_{\mathrm{outlet}}\right)} \tag{8}$$

$$q_{ij} = C_{ij}^{\mathrm{eff}}(T_i - T_j) \tag{9}$$

where q_{ij} is heat flux density, L is the distance from the inlet to the outlet, and A is the cross-sectional area of the cubic sample. T_{inlet} and T_{outlet} are the constant temperatures in the inlet and outlet, respectively.

2.3 *Materials and parameters*

This investigation establishes the material parameters for glass beads in the DEM model through calibration against hollow cylinder torsional shear test data reported by Yang et al. (2015). The calibration process employed an iterative trial-and-error approach, yielding the following optimized parameters for glass beads: Young's modulus of 50 GPa, Poisson's ratio of 0.15, and intrinsic friction coefficient of 0.6. The particle density was adopted as 2500 kg/m³ based on previous work by Sarkar et al. (2019). As demonstrated in Figure 4, the numerical simulations show excellent correspondence with experimental data, confirming the validity of the calibrated DEM parameters in representing the actual mechanical behavior of glass beads.

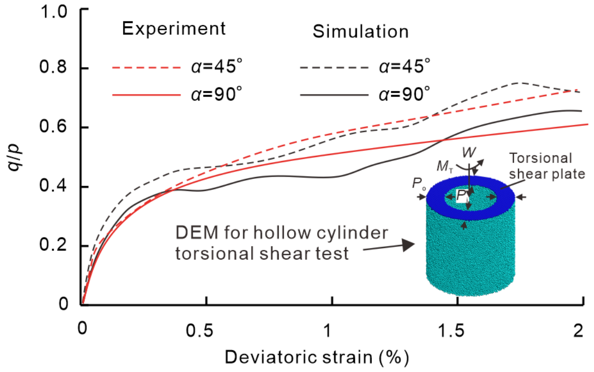

Figure 4. Glass beads' parameters calibration by hollow cylinder torsional shear test.

3 RESULTS AND DISCUSSION

This investigation comprehensively examines how PSR interacts with various stress-state parameters (including the intermediate principal stress ratio b and mean principal stress p) and microstructural characteristics (such as porosity n and particle size ratio $d_{\max}/d_{\min}$), and the influence on the effective thermal conduction properties of granular materials.

3.1 *Principal stress rotation*

The response of granular materials to PSR plays a pivotal role in determining their thermo-mechanical characteristics. Figure 5 demonstrates that all specimens exhibit progressively increasing volumetric strain during PSR, revealing a distinct contraction tendency. This compressive behavior aligns with established experimental findings from multiple PSR studies (Al-rkaby et al., 2017).

The magnitude of contraction shows positive correlation with both *b*-value and *n*-value parameters, with *n* demonstrating particularly dominant control. In contrast, dilatational behavior diminishes with rising *p* and $d_{\max}/d_{\min}$, with these two factors exhibiting comparable influence levels.

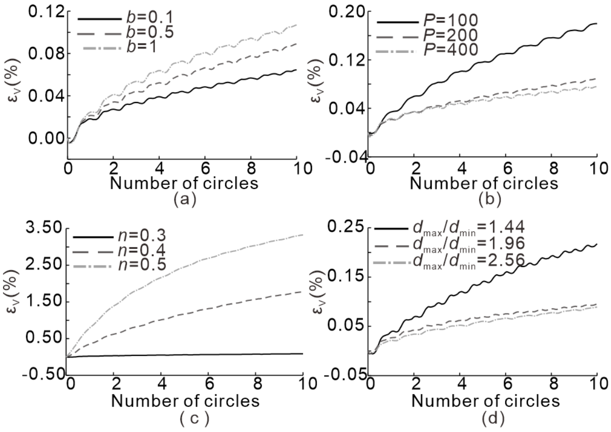

Figure 5. Response of different parameters to volumetric strain: (a) Effect of *b*, (b) Effect of *P*, (c) Effect of *n*, and (d) Effect of $d_{\max}/d_{\min}$.

The results presented above are obtained from simulations with a total of approximately 6 million time steps, a condition that ensures quasi-static loading. To evaluate the influence of simulation duration on the results, PSR processes were simulated under different total time steps. As shown in Figure 6, the volumetric strain is significantly smaller at 3 million steps, while the results at 6 million and 9 million steps show negligible differences. Therefore, the selection of 6 million steps is justified as it ensures numerical stability and computational efficiency.

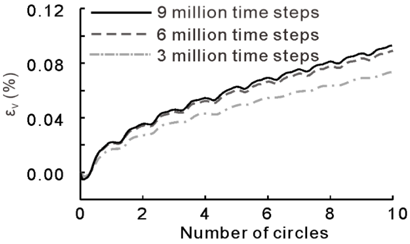

Figure 6. Influence of the total time steps on the simulation results

3.2 *Thermal conductivity*

PSR consistently enhances directional thermal conductivity across all principal axes (X, Y, Z), independent of variations in *b*, *p*, *n*, or $d_{\max}/d_{\min}$ (Figure 7). The parametric influences exhibit distinct directional characteristics, as follows. **Effect of *b*** (Figure 7a): The X and Y-direction conductivity demonstrates greater sensitivity to *b* variations compared to the Z-direction, as evidenced by steeper response curves. **Effect of *p*** (Figure 7b): Higher *p* elevates k_{eff} in all directions because lower *p* values during partial consolidation yield looser pore configurations. **Effect of *n*** (Figure 7c): Lower *n* values correspond to higher k_{eff}. In addition, the k_{eff} variation rate accelerates with increasing *n* values, as evidenced by steeper response curves. **Effect of $d_{\max}/d_{\min}$** (Figure 7d): Larger size disparities promote k_{eff} enhancement through improved pore-filling by finer particles, creating additional thermal pathways.

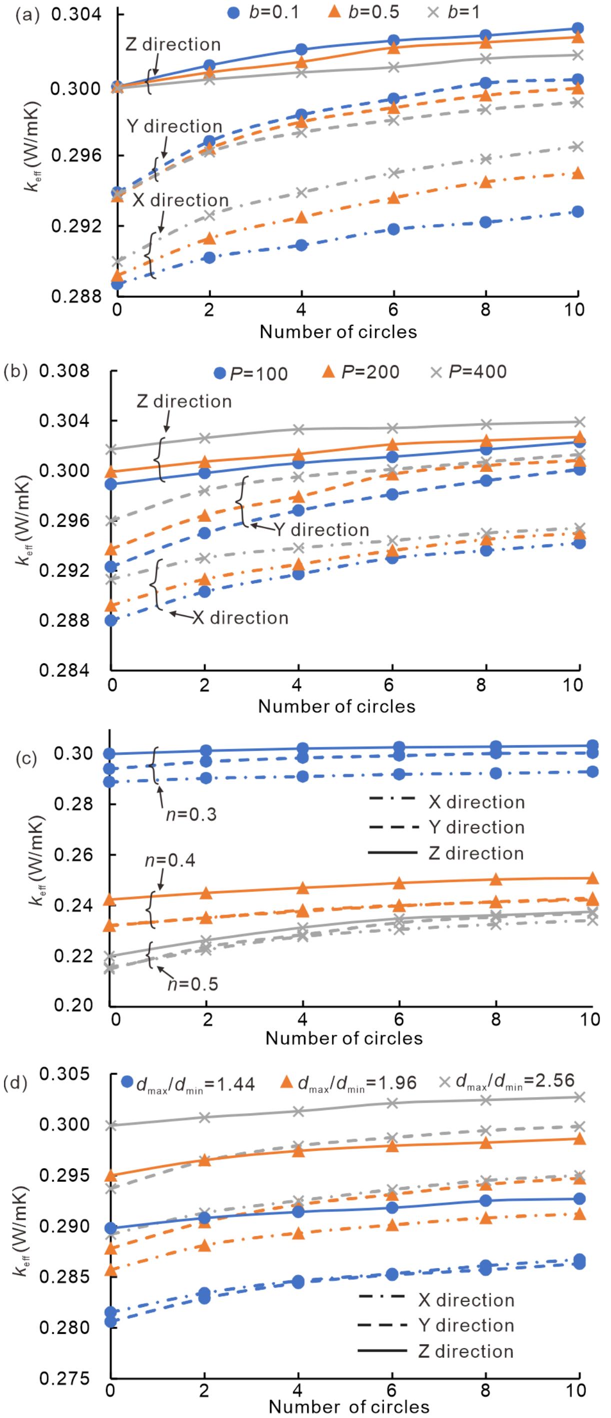

Figure 7. Response of different parameters to effective thermal conductivity in X, Y and Z directions: (a) Effect of *b*, (b) Effect of *P*, (c) Effect of *n*, and (d) Effect of $d_{\max}/d_{\min}$.

To provide deeper insight into the anisotropic response induced by PSR, Figure 8 presents the directional distributions of both contact forces and thermal conduction pathways during the 10th loading cycle. Key observations reveal that: (i) The major axis of contact force directional distribution follows the rotational trajectory of the σ_1 axis during PSR; (ii) Thermal pathway orientations maintain their initial configuration without significant angular deviation. This compelling evidence demonstrates that PSR exclusively governs the anisotropic evolution of interparticle contact forces, while exerting negligible influence on the directional characteristics of thermal transfer networks.

The impact of PSR on k_{eff} can be examined through analysis of the second-order fabric anisotropy tensor. Figure 9 demonstrates that both S-S and S-F-S thermal path anisotropies exhibit minor fluctuations during PSR, their magnitudes remain substantially lower than contact force anisotropies. Notably, S-S paths display marginally greater anisotropy compared to S-F-S paths, suggesting particle-to-particle contacts play a more dominant role in governing thermal path orientation. The anisotropy of all thermal paths shows minimal variation. This observation explains why the distribution density of all thermal conduction pathways remains unchanged during PSR, as demonstrated in Figure 7.

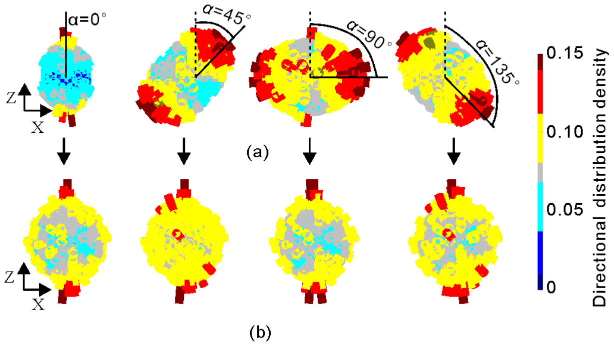

Figure 8. Contact force and thermal conductance paths distribution density: (a) Contact force distribution, and (b) All thermal conductance paths distribution.

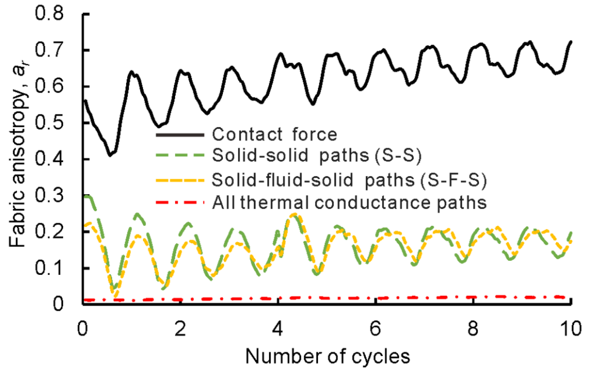

Figure 9. Evolution of the fabric anisotropy with the number of cycles

To further elucidate the enhancement mechanism of PSR on thermal conductivity. Figure 10 illustrates the evolutionary pattern of thermal conduction paths under varying particle size ratios $d_{\mathrm{max}}/d_{\mathrm{min}}$. Before PSR initiation, S-F-S paths substantially outnumber S-S paths.

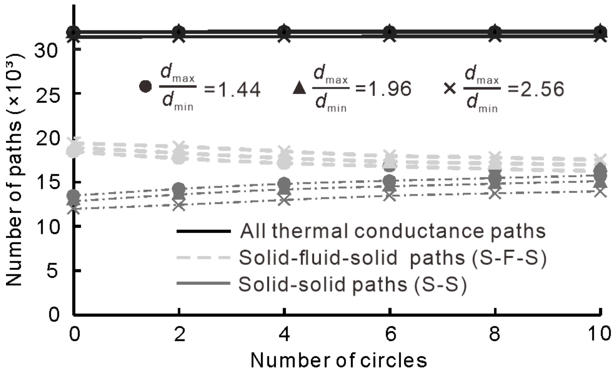

Figure 10. Variation trend of thermal conductance paths during the process of rotation.

Throughout the rotational loading, a progressive reduction in S-F-S paths occurs alongside a corresponding increase in S-S paths. Notably, the aggregate pathway quantity shows minimal variation, suggesting compressive sample deformation converts S-F-S into S-S paths. This conversion mechanism enhances effective thermal conductivity while preserving negligible fabric anisotropy in the overall thermal network.

4 CONCLUSION

The main conclusions of this paper are as follows:

Principal stress rotation (PSR) induces volumetric contraction, with shrinkage magnitude positively correlated to the intermediate principal stress ratio *b* and porosity *n* (*n* being most influential), but inversely related to the mean principal stress *p* and particle size ratio $d_{\mathrm{max}}/d_{\mathrm{min}}$. Thermally, PSR universally enhances effective thermal conductivity k_{eff} across all axes (X/Y/Z), though directional responses vary: higher *b* reduces Z/Y-direction k_{eff} while increasing X-direction values, whereas elevated *p* and $d_{\mathrm{max}}/d_{\mathrm{min}}$ or reduced *n* generally boost k_{eff} in all directions.

Microstructurally, Z-direction maintains maximum k_{eff} followed by Y then X throughout PSR, with anisotropy established during initial consolidation rather than rotation. The k_{eff} improvement stems from S-F-S to S-S path conversion without all pathway quantity change, preserving the existing anisotropy while uniformly elevating conductivity.

5 ACKNOWLEDGEMENTS

This research was sponsored by the National Natural Science Foundation of China (Grant No. 52478339).

6 REFERENCES

Al-Rkaby, A. H. J., Chegenizadeh, A. & Nikraz, H. R. 2017. Cyclic behavior of reinforced sand under principal stress rotation. *Journal of Rock Mechanics and Geotechnical Engineering,* 9, 585-598.

Cerfontaine, B., Ciantia, M., Brown, M. J. & Sharif, Y. U. 2021. DEM study of particle scale and penetration rate on the installation mechanisms of screw piles in sand. *Computers and Geotechnics,* 139.

Fei, W. & Narsilio, G. A. 2022. Estimation of thermal conductivity of cemented sands using thermal network models. *Journal of Rock Mechanics and Geotechnical Engineering,* 14, 210-218.

Liu, Y., Mao, H., Xu, C. & Zhang, Y. 2021. DEM investigation on the mechanical behavior of mudstone in the hollow cylinder torsional shear test. *Computers and Geotechnics,* 137

Sarkar, D., König, D. & Goudarzy, M. 2019. The influence of particle characteristics on the index void ratios in granular materials. *Particuology,* 46, 1-13.

Yang, Y., Fei, W., Yu, H., Ooi, J. & Rotter, M. 2015. Experimental study of anisotropy and non-coaxiality of granular solids. *Granular Matter,* 17, 189-196.

Yun, T. S. & Evans, T. M. 2010. Three-dimensional random network model for thermal conductivity in particulate materials. *Computers and Geotechnics,* 37, 991-998.

Zhou, A., Li, P., Fan, L., Yi, Z., Tang, X. & Fei, W. 2025. Influence of drainage system on the stability of underground CAES gas storage under different lateral pressure coefficients. *Tunnelling and Underground Space Technology,* 159.

Zueter, A. F., Newman, G. & Sasmito, A. P. 2021. Numerical study on the cooling characteristics of hybrid thermosyphons: Case study of the Giant Mine, Canada. *Cold Regions Science and Technology,* 189.